Origin of robust nanoscale ferromagnetism in Fe-doped Ge revealed by angle-resolved photoemission spectroscopy and first-principles calculation

S. Sakamoto,[1] Y. K. Wakabayashi,[2] Y. Takeda,[3] S.-i. Fujimori,[3] H. Suzuki,[1] Y. Ban,[2] H. Yamagami,[3,4] M. Tanaka,[2,5] S. Ohya,[2,5] and A. Fujimori[1]

[1]*Department of Physics, The University of Tokyo, Bunkyo-ku, Tokyo 113-0033, Japan*

[2]*Department of Electrical Engineering and Information Systems, The University of Tokyo, Bunkyo-ku, Tokyo 113-8656, Japan*

[3]*Materials Sciences Research Center, Japan Atomic Energy Agency (JAEA), Sayo-gun, Hyogo 679-5148, Japan*

[4]*Department of Physics, Kyoto Sangyo University, Kyoto 603-8555, Japan*

[5]*Center for Spintronics Research Network, The University of Tokyo, Bunkyo-ku, Tokyo 113-8656, Japan*

(Received 20 May 2016; revised manuscript received 27 December 2016; published 8 February 2017)

$Ge_{1-x}Fe_x$ (Ge:Fe) shows ferromagnetic behavior up to a relatively high temperature of 210 K and hence is a promising material for spintronic applications compatible with Si technology. Unlike the prototypical system (Ga,Mn)As where itinerant holes induce long-range ferromagnetic order of the Mn spins, however, its ferromagnetism evolves from robust nanoscale ferromagnetic domains formed in Fe-rich regions. We have studied its underlying electronic structure by soft x-ray angle-resolved photoemission spectroscopy measurements and first-principles supercell calculation. We observed finite Fe 3*d* components in the states at the Fermi level (E_F) in a wide region of momentum space, and the E_F was located ∼0.35 eV above the valence-band maximum of the host Ge. Our calculation indicates that the E_F is also within the deep acceptor-level impurity band induced by the strong p-$d(t_2)$ hybridization. We conclude that the additional minority-spin $d(e)$ electron characteristic of the Fe^{2+} state is responsible for the short-range ferromagnetic coupling between Fe atoms, making the magnetism markedly different from that of (Ga,Mn)As.

DOI: 10.1103/PhysRevB.95.075203

I. INTRODUCTION

Ferromagnetic semiconductors (FMSs) such as (Ga,Mn)As [1,2] have attracted much attention both from scientific and technological points of view [3–8]. Group-IV FMSs are particularly important because they are compatible with mature Si-based technology. $Ge_{1-x}Fe_x$ (Ge:Fe) is a promising material [9–12] and indeed can be grown epitaxially on Ge and Si substrates by the low-temperature molecular beam epitaxy (LT-MBE) method without the formation of intermetallic precipitates [13]. The Curie temperature (T_C) increases with the Fe content and with the inhomogeneity of Fe-atom distribution [11,12] and reaches ∼210 K at its highest by postgrowth annealing [11], which is above the highest T_C of (Ga,Mn)As, ∼200 K [14]. Unlike (Ga,Mn)As, where the T_C is intimately related to the carrier concentration or the hole conductivity, the T_C does not depend on carrier concentration in Ge:Fe [13], and the conductivity remains low upon Fe doping. A recent x-ray magnetic circular dichroism (XMCD) study [15] has revealed that the ferromagnetic order evolves from nanoscale ferromagnetic domains formed in Fe-rich regions, which are robust enough to persist even at room temperature.

In order to explain the origin of the ferromagnetism in (Ga,Mn)As and related FMSs, two models have been proposed so far [5,16,17], namely, the valence-band model [18,19] and the impurity-band model [20–23]. In the valence-band model, acceptor levels derived from the magnetic impurities are merged into the valence band and itinerant holes occupying states around the valence-band maximum (VBM) mediate ferromagnetism through Zener's p-d exchange mechanism. In the case of the impurity-band model, on the other hand, impurity levels are detached from the VBM and lie within the band gap of the host semiconductor and hence ferromagnetism is stabilized through a double-exchange-like mechanism within the impurity band.

In this study, we have elucidated the origin of the unique magnetic properties of Ge:Fe distinct from those of (Ga,Mn)As by examining its electronic structure, especially the position of the Fermi level (E_F) and the modification of the host band structure caused by the Fe 3*d* electrons using soft x-ray angle-resolved photoemission spectroscopy (SX-ARPES) and first-principles supercell calculations.

II. EXPERIMENT

A $Ge_{0.935}Fe_{0.065}$ film was synthesized using the LT-MBE method at the growth temperature of 240 °C. The structure of the sample was, from the top surface to the bottom, Ge cap (∼2 nm)/$Ge_{0.935}Fe_{0.065}$ (∼120 nm)/Ge buffer (∼30 nm)/p-Ge (001) substrate. Note that the sample structure and the growth condition were the same as those reported in Refs. [12,15], and the sample is expected to have an inhomogeneous distribution of Fe atoms maintaining the diamond lattice structure and to show nanoscale ferromagnetism above the T_C of 100 K [12,15]. In the Fe-rich regions, the Fe content would be about 10%, while in the Fe-poor regions, ∼4% [12].

The SX-ARPES experiment was performed at beam line BL23SU of SPring-8. The sample temperature was set to 20 K and circularly polarized x rays of 700–950 eV were used. The energy resolution was about 170 meV. The sample was placed so that the [−110] direction became parallel to the analyzer slit and perpendicular to the beam. By rotating the sample around the [−110] axis and changing the photon energy, we were able to cover the entire Brillouin zone. X-ray absorption spectra were taken in the total electron yield mode. In order to remove the oxidized surface layer, just before loading the sample

into the vacuum chamber of the spectrometer, we etched the sample in a hydrofluoric acid (HF) solution (3 mol/L) for 5 s and subsequently rinsed it in water, which is known to be an efficient way to clean the surfaces of Ge [24] as well as those of Ge:Fe [15].

First-principles supercell calculations were done based on the density functional theory (DFT) utilizing the full-potential augmented-plane-wave method implemented in the WIEN2K package [25]. For the calculation of the host Ge band structure, a modified Becke-Johnson (mBJ) exchange potential with the local density approximation (LDA) for correlation potential [26] was employed. For the calculation of the spin-resolved partial density of states (PDOS) of Fe $3d$ in Ge, we constructed the $3 \times 3 \times 3$ supercell consisting of 53 Ge atoms and 1 Fe atom, and the cubic unit cell consisting of 7 Ge atoms and 1 Fe atom. We used the generalized gradient approximation (GGA) of the Perdew-Burke-Ernzerhof type [27] for the exchange-correlation energy functional. The experimental lattice constant of $a = 5.648$ Å for $Ge_{0.935}Fe_{0.065}$ [12] was used and spin-orbit interaction was included for all the calculations.

III. RESULTS AND DISCUSSION

Figure 1(a) shows resonance photoemission spectroscopy (RPES) spectra taken in the angle-integrated mode at 0.5-eV photon-energy intervals in the Fe L_3 absorption-edge region. Here, the off-resonance spectrum taken at a lower photon energy of 704 eV has been subtracted. The colors of the spectra correspond to that of the open circles on the x-ray absorption spectroscopy (XAS) spectra in Fig. 1(c) and indicate photon energies. Note that the binding energy is defined relative to E_F. One can see a strong normal Auger peak dispersing with photon energy in the spectra. This indicates the itinerant nature of the Fe $3d$ electrons in Ge:Fe, because the normal Auger process takes place when the core-hole potential is screened by conduction electrons faster than core-hole decay. The itinerant nature of the Fe $3d$ electrons is further confirmed by the XAS spectra consisting of a broad single peak without multiplet structure seen when $3d$ electrons are localized [28]. It should be noted that the XAS spectrum does not show Fe^{3+} oxide signals, which guarantees the effectiveness of the HF etching prior to the measurements. In addition to the normal Auger peak, a nondispersive feature can be seen around the binding energy of 4 eV denoted by a dashed line and exhibits resonance enhancement. (How the dispersive and nondispersive features coexist in the spectra are summarized in Fig. S1 [29].) Such a structure with a constant binding energy is due either to direct recombination, where the photoexcited electron recombines with the core hole, or to a satellite [30], where the photoexcited core electron acts as a spectator to the core-hole recombination process.

Figure 1(d) shows the same RPES spectra plotted on an expanded scale. Due to the strong Auger peak, it was difficult to extract the the PDOS from the spectra taken with the photon energy of the absorption peak at 708 eV. Therefore, by using higher-energy photons of 714 eV, we have deduced the Fe $3d$ PDOS as shown by a red curve in Fig. 1(d). The PDOS is broad, extending from E_F to 5 eV below it, out of which the structure around 4 eV is attributed to a satellite because it showed

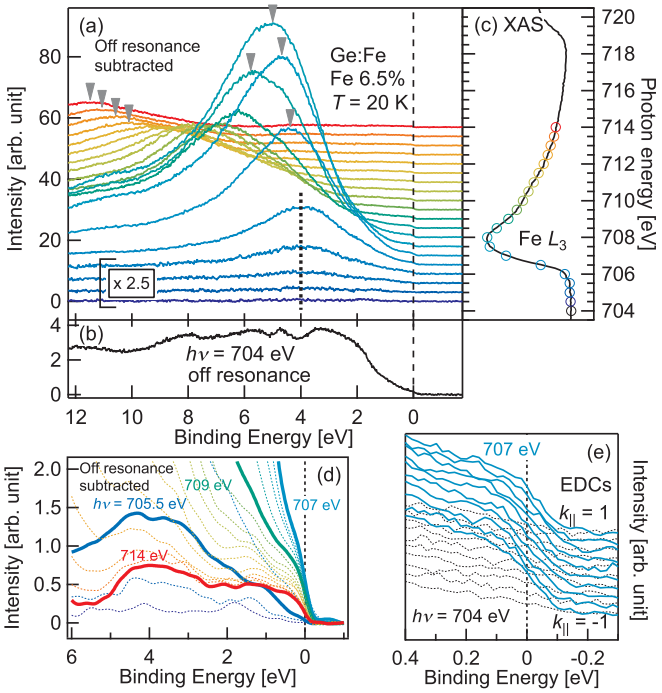

FIG. 1. Resonance photoemission spectra of $Ge_{0.9335}Fe_{0.065}$. (a) Spectra taken in the angle-integrated mode across the Fe L_3 absorption edge at 0.5 eV photon-energy interval as depicted by circles on the x-ray absorption spectrum in (c). The color of the open circles in (c) corresponds to that of the spectra in (a). The off-resonance spectrum (b) has been subtracted from all the spectra in (a), where the units of the vertical axes in (a) and (b) are the same. Triangles show the position of the normal Auger peak. The spectra for $h\nu = 704.5$–706 eV have been magnified by a factor of 2.5. (d) Enlarged plot of the spectra in (a). The same color as in (a) is used. (e) Energy distribution curves taken in the angle-resolved mode along $k_{||} \parallel [-110]$, where $k_{||}$ is in units of $2\sqrt{2}\pi/a$.

strong enhancement at the resonance energy like the satellite in transition metals and transition-metal compounds listed in the Supplemental Material [29]. Therefore, we consider that the main part of the Fe $3d$ PDOS is located from E_F to ~3 eV below it. In addition, there can be seen the Fermi edgelike step at E_F, which indicates that the Fe $3d$ states have a finite contribution to the states at E_F and are involved in the charge transport of Ge:Fe. Figure 1(e) shows the energy distribution curves (EDCs) taken in the angle-resolved mode at the photon energies of 704 eV (off resonance) and 707 eV (on resonance). The enhanced Fe $3d$ states were found to exist in a wide region in momentum space without appreciable dispersions. Note that the Fermi edgelike feature at E_F is much clearer in Ge:Fe than in (Ga,Mn)As [31], indicating that contributions of $3d$ electrons to states at E_F are more pronounced in Ge:Fe than in (Ga,Mn)As.

Figure 2(a) shows the photon energy dependence of ARPES spectra at the binding energy of 4 eV around the Γ point, from which one can see that the ARPES taken with x rays of 875 eV crosses the Γ point. In Fig. 2(b), the maximum energy of the valence-band dispersion is plotted against photon energy and reaches the VBM at ~876 eV. The energy of the VBM thus deduced is found to be 0.35 eV below E_F, indicating that the

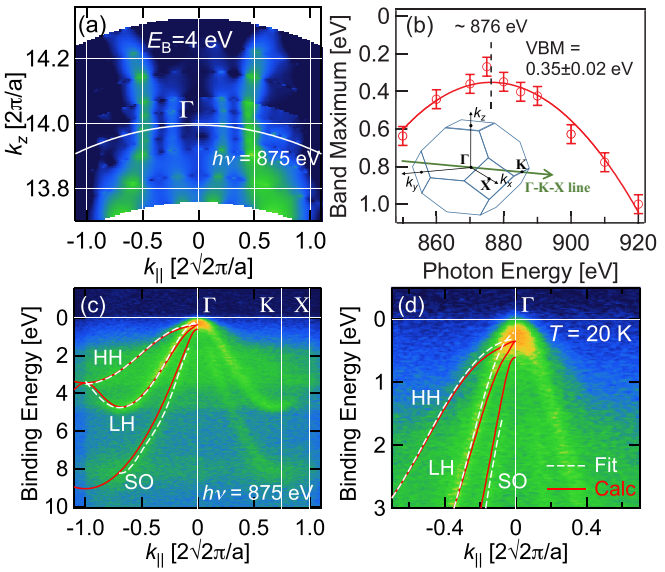

FIG. 2. ARPES band mapping for $Ge_{0.935}Fe_{0.065}$. (a) $k_{||}$-k_z mapping image at the binding energy of 4 eV. A white curve represents the ARPES cut for the photon energy of 875 eV. (b) Maximum of the band dispersion along $k_{||}$ as a function of photon energy. The solid curve represents a fitted parabolic function. The inset shows the Brillouin zone of the fcc lattice. (c), (d) ARPES spectra along the Γ-K-X line taken with $h\nu = 875$ eV. The peak positions of the second derivatives of the energy distribution curves have been fitted to a Fourier series and are shown by dashed curves. Solid curves represent the calculated band dispersions of the host Ge, where the heavy-hole (HH) band, the light-hole (LH) band, and the split-off (SO) band can be seen.

Fermi level of Ge:Fe is located in the middle of the Ge band gap of ∼0.7 eV.

Figures 2(c) and 2(d) show ARPES spectra along the Γ-K-X line in the Brillouin zone of the fcc lattice [see the inset of Fig. 2(b)] taken with the photon energy of 875 eV. The peak positions of the second derivatives of the EDCs have been fitted to a Fourier series and are shown by dashed curves. Here, clear band dispersions characteristic of Ge, such as the heavy-hole (HH) band, the light-hole (LH) band, and the split-off (SO) band, can be seen, which indicates the good crystallinity of the Ge:Fe sample as well as the good quality of the sample surface after the HF etching. Solid curves represent the calculated band dispersions of the Ge host. As can be seen from Fig. 2, the ARPES spectra of Ge:Fe agree fairy well with the calculated band dispersions of Ge within the resolution of the present setup, indicating that the doped Fe atoms did not affect the electronic structure of the Ge host significantly. Note that the observed band structure would reflect contributions more from the Fe-poor regions (4%) than the Fe-rich (10%) regions for the following reasons: the volume of the Fe-poor regions is larger than that of the Fe-rich regions by ∼20% in the present 6.5% Fe-doped sample, and the band structure of the Fe-rich regions is more strongly perturbed and should be more obscured than that of the Fe-poor regions. Insensitivity of the band structure to transition-metal doping was also found in the previous SX-ARPES and vacuum ultraviolet (VUV)-ARPES studies on GaMnAs [31,32], although whether the energy bands are shifted with doping or not remains controversial.

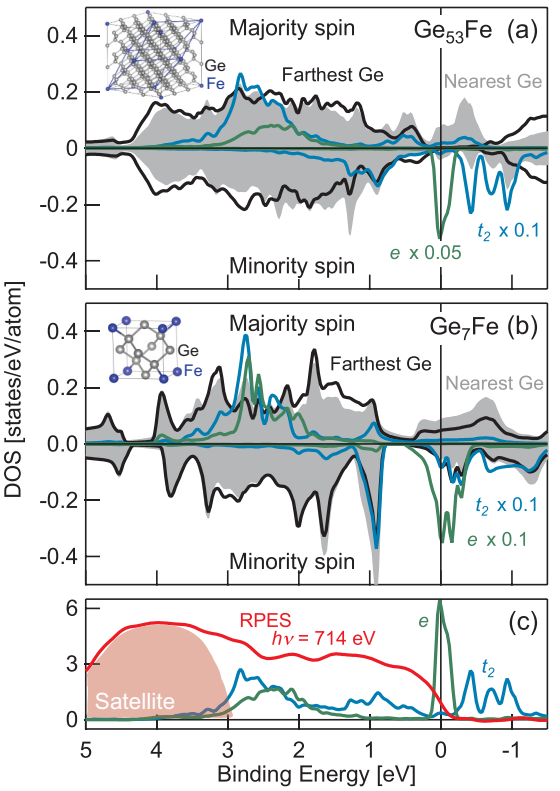

FIG. 3. Spin-resolved PDOS of (a) $Ge_{53}Fe$ and (b) Ge_7Fe supercells. The supercells are illustrated in the upper-left corner of each panel [33], and the primitive cell of $Ge_{53}Fe$ is indicated by blue lines inside the cubic cell. The black curves and gray area represent the PDOS of the farthest and the nearest Ge atom to the Fe atom, respectively, and blue and green curves represent the PDOS of the Fe $3d(t_2)$ and $3d(e)$ states of Fe, respectively. The PDOS of the t_2 and e states have been scaled by a factor of 0.05 or 0.1 for the sake of comparison with the PDOS of Ge. (c) Spin-averaged PDOS of the Fe $3d(t_2)$ and $3d(e)$ orbitals of the $Ge_{53}Fe$ supercell. The experimental spectrum is superposed by a red curve.

In order to examine the electronic structure of an Fe atom substituting a Ge atom in the Ge host in comparison with a Mn atom substituting Ga in the GaAs host, we have calculated the spin-resolved PDOS of the $Ge_{53}Fe$ supercell (Fe 1.85%), where one Fe atom exists in a $3 \times 3 \times 3$ supercell, and of the Ge_7Fe supercell (Fe 12.5%), where one Fe atom exists in the cubic unit cell, as shown in Figs. 3(a) and 3(b), respectively. Since Fe-rich (10%) and Fe-poor (4%) regions coexist in the real system [12], the calculated electronic structures of $Ge_{53}Fe$ would explain the properties of the Fe-poor regions, and those of Ge_7Fe the Fe-rich regions. Although the situation is different in the real system, in which Fe atoms are randomly distributed, to study the supercells is a good starting point to elucidate the underlying physics. In Figs. 3(a) and 3(b), the black curve and gray area represent the PDOS of the farthest and the nearest Ge atoms to the Fe atom, and blue and green curves represent the PDOS of Fe $3d(t_2)$ and $3d(e)$ orbitals, respectively.

In the case of $Ge_{53}Fe$ [Fig. 3(a)], the PDOS of the farthest Ge is not affected by the presence of Fe significantly, which means that the Fe atom in this supercell can be considered an isolated impurity. On the other hand, the PDOS of the nearest

Ge is strongly affected by hybridization with Fe $3d$ states [mainly with Fe $3d(t_2)$ states], in particular within ∼0.5 eV of E_F, as in the case of (Ga,Mn)As. A significant difference between Ge:Fe and (Ga,Mn)As is that there is an additional Fe $3d$ electron in Ge:Fe which occupies the minority-spin $3d(e)$ states at the Fermi level. This means that Fe is in the Fe^{2+} state with $3d^6(sp)^2$ configuration, consistent with a previous calculation on a $2 \times 2 \times 2$ Ge supercell having a neighboring Fe-Fe pair [34]. [In that calculation, the $3d(e)$ state was split into bonding and antibonding states due to the overlap of the d orbitals of paired Fe atoms.] In addition, the p-$d(t_2)$ hybridized states in Ge:Fe are pushed from the VBM into the band gap of host Ge and act as deep acceptor levels, which agrees with the experimental finding that the Fermi level was deep inside the band gap.

In the case of Ge_7Fe [Fig. 3(b)], the PDOS of both nearest and farthest Ge atoms are significantly modified by Fe atoms due to the high concentration of Fe. The bandwidths of the Fe $3d$ levels and p-d hybridized levels in Ge_7Fe are broader than those of $Ge_{53}Fe$ especially near and above the Fermi level due to the shorter Fe-Fe distance. It should be mentioned, however, that the relative positions of different Fe $3d$ levels in Ge_7Fe are the same as those in $Ge_{53}Fe$, and the basic electronic structures are not altered qualitatively.

Figure 3(c) shows the spin-averaged PDOS of Fe $3d(t_2)$ and $3d(e)$ orbitals of $Ge_{53}Fe$ in comparison with the experimentally obtained PDOS. Except for the structure around 4 eV, which we attribute to a satellite, the calculated PDOS agrees well with the experiment at least qualitatively; that is, both PDOS have a finite value at E_F and extend down to ∼3 eV below E_F.

A schematic energy-level diagram of the electronic structure of the Fe atom in the Ge matrix thus obtained is shown in Fig. 4(a) and that of the Mn atom in the GaAs matrix in Fig. 4(b). In both cases, due to the T_d local crystal symmetry around the transition-metal atom, the d levels are split into two sublevels, the doubly degenerate $3d(e)$ level and the triply degenerate $3d(t_2)$ level. In the presence of p-d hybridization [predominantly p-$d(t_2)$ hybridization], the majority-spin $3d(t_2)$ levels are shifted downwards and the minority-spin t_2 levels upwards. At the same time, some p states are split from the VBM: majority-spin levels are shifted upward and minority-spin ones downward. Note that, as a result of the p-$d(t_2)$ hybridization, the shifted levels have both $d(t_2)$ and p characters, where in Fig. 4 the states with predominant $d(t_2)$ and p character are indicated by gray and green boxes, respectively, and, therefore, we refer to the lower levels as bonding levels and the upper as antibonding levels hereafter. In the case of (Ga,Mn)As, the majority-spin d levels are fully occupied and the minority-spin d levels are empty. Mn takes the Mn^{2+} state with five majority-spin d electrons and one p hole enters the valence band. Due to the strongest Hund coupling of the Mn^{2+} state with d^5 configuration, the majority-spin d levels are located well below E_F, while the minority-spin d levels are located well above E_F. Therefore, the hole enters the majority-spin antibonding levels with predominant p characters split off from the VBM and acts as a shallow acceptor level. On the other hand, from the electron counting argument [29], the Fe atom substituting Ge should have six d electrons and provides two p holes. The majority-spin d levels of Ge:Fe are shallower in energy than those of (Ga,Mn)As because of the reduced Hund energy, and p-$d(t_2)$ hybridization becomes stronger. As a result, the majority-spin antibonding levels are pushed well above the VBM compared to the Mn case and even above the minority-spin $3d(e)$ level. Therefore, the sixth d electrons of Fe occupy the doubly degenerate minority-spin $3d(e)$ states and the two p holes reside in the majority-spin states of the deep acceptor-level origin. If the Fe concentration is high enough and Fe-Fe interaction is non-negligible, the bandwidths of the Fe $3d$ levels including the minority-spin $3d(e)$ level become broader as mentioned above and shown in Fig. 3(b). Accordingly, since the minority-spin $3d(e)$ band is almost half filled, the double-exchange mechanism would become effective. This is probably the case for the Fe-rich regions in this material.

From the above considerations, we conclude that the valence-band model is not applicable in a different sense from the (Ga,Mn)As case. The majority-spin p-$d(t_2)$ hybridized levels located above the VBM appear responsible for the charge transport and the nondispersive Fe $3d$ intensity at E_F observed by the resonance ARPES measurements. On the other hand, the narrow-band or nearly localized Fe $3d(e)$ electrons play an essential role in stabilizing the ferromagnetism most likely through a double-exchange-like mechanism between neighboring Fe atoms. The present picture explains the

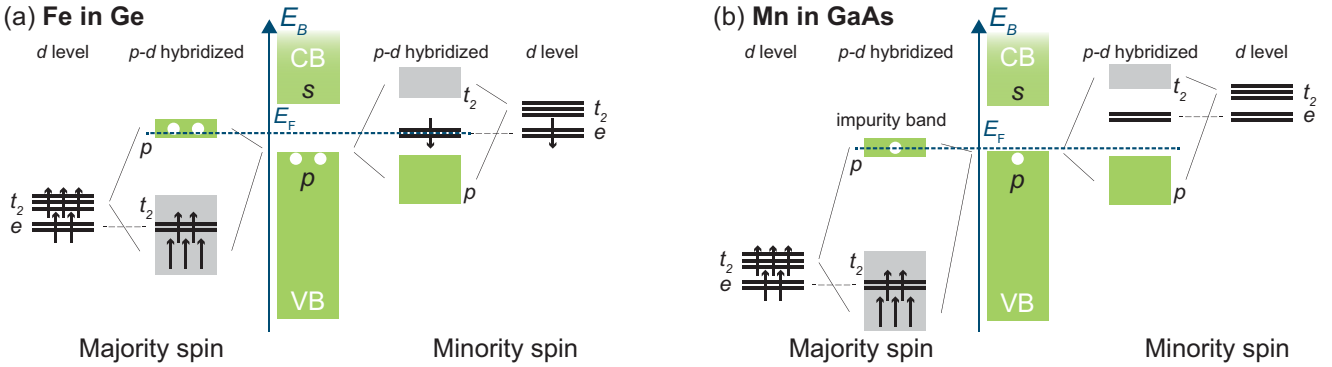

FIG. 4. Schematic energy-level diagram of (a) Ge:Fe and (b) (Ga,Mn)As. At the center of each panel, the valence band (VB) and the conduction band (CB) of the host semiconductor are shown. At the left- and right-hand sides of each panel, the majority-spin and minority-spin d levels are shown, respectively. In addition, energy levels with p-d hybridization are shown in between, where green and gray boxes represent the state with predominant p and t_2 character, respectively.

observed increase of T_C with Fe concentration [9] and with the inhomogeneity of Fe distribution [11,12]. The same picture explains the observation of robust nanoscale ferromagnetic domains formed in Fe-rich regions well above the T_C [15].

IV. SUMMARY

In summary, we have performed SX-ARPES measurements and first-principles supercell calculation on Ge:Fe. ARPES spectra show that the Fermi level is located at 0.35 eV above the VBM and that nondispersive Fe 3*d* states exist at the Fermi level, which can be attributed to majority-spin p-$d(t_2)$ antibonding states of deep acceptor-level origin, and also to minority-spin Fe $3d(e)$ states. Combining the ARPES result with the results of supercell calculations and the previous XMCD study, it is concluded that charge transport occurs through the majority-spin impurity band of the deep acceptor-level origin, and that the ferromagnetic interaction is mediated by double-exchange interaction within the nearly localized minority-spin Fe $3d(e)$ band.

ACKNOWLEDGMENTS

This work was supported by Grants-in-Aid for Scientific Research from the JSPS (Grants No. 15H02109, No. 23000010, and No. 26249039). The experiment was done under the Shared Use Program of JAEA Facilities (Proposal No. 2014B-E29) with the approval of the Nanotechnology Platform Project supported by MEXT. The synchrotron radiation experiments were performed at the JAEA beamline BL23SU in SPring-8 (Proposal No. 2014B3881). A.F. is an adjunct member of the Center for Spintronics Research Network (CSRN), the University of Tokyo, under Spintronics Research Network of Japan (Spin-RNJ). S.S. acknowledges financial support from the Advanced Leading Graduate Course for Photon Science (ALPS), and Y.K.W. acknowledges financial support from the Materials Education program for the future leaders in Research, Industry, and Technology (MERIT). H.S. and Y.K.W. acknowledge financial support from the JSPS Research Fellowship for Young Scientists.

[1] H. Ohno, A. Shen, F. Matsukura, A. Oiwa, A. Endo, S. Katsumoto, and Y. Iye, Appl. Phys. Lett. **69**, 363 (1996).
[2] H. Ohno, Science **281**, 951 (1998).
[3] S. A. Wolf, D. D. Awschalom, R. A. Buhrman, J. M. Daughton, S. von Molnár, M. L. Roukes, A. Y. Chtchelkanova, and D. M. Treger, Science **294**, 1488 (2001).
[4] I. Žutić, J. Fabian, and S. Das Sarma, Rev. Mod. Phys. **76**, 323 (2004).
[5] T. Dietl, Nat. Mater. **9**, 965 (2010).
[6] T. Dietl and H. Ohno, Rev. Mod. Phys. **86**, 187 (2014).
[7] T. Jungwirth, J. Wunderlich, V. Novák, K. Olejník, B. L. Gallagher, R. P. Campion, K. W. Edmonds, A. W. Rushforth, A. J. Ferguson, and P. Němec, Rev. Mod. Phys. **86**, 855 (2014).
[8] M. Tanaka, S. Ohya, and P. Nam Hai, Appl. Phys. Rev. **1**, 011102 (2014).
[9] Y. Shuto, M. Tanaka, and S. Sugahara, J. Appl. Phys. **99**, 08D516 (2006); Appl. Phys. Lett. **90**, 132512 (2007).
[10] Y. K. Wakabayashi, K. Okamoto, Y. Ban, S. Sato, M. Tanaka, and S. Ohya Appl. Phys. Express **9**, 123001 (2016).
[11] Y. K. Wakabayashi, Y. Ban, S. Ohya, and M. Tanaka, Phys. Rev. B **90**, 205209 (2014).
[12] Y. K. Wakabayashi, S. Ohya, Y. Ban, and M. Tanaka, J. Appl. Phys. **116**, 173906 (2014).
[13] Y. Ban, Y. Wakabayashi, R. Akiyama, R. Nakane, and M. Tanaka, AIP Adv. **4**, 097108 (2014).
[14] L. Chen, X. Yang, F. Yang, J. Zhao, J. Misuraca, P. Xiong, and S. von Molnár, Nano Lett. **11**, 2584 (2011).
[15] Y. K. Wakabayashi, S. Sakamoto, Y.-h. Takeda, K. Ishigami, Y. Takahashi, Y. Saitoh, H. Yamagami, A. Fujimori, M. Tanaka, and S. Ohya, Sci. Rep. **6**, 23295 (2016).
[16] T. Jungwirth, J. Sinova, J. Mašek, J. Kučera, and A. H. MacDonald, Rev. Mod. Phys. **78**, 809 (2006).
[17] K. Sato, L. Bergqvist, J. Kudrnovský, P. H. Dederichs, O. Eriksson, I. Turek, B. Sanyal, G. Bouzerar, H. Katayama-Yoshida, V. A. Dinh, T. Fukushima, H. Kizaki, and R. Zeller, Rev. Mod. Phys. **82**, 1633 (2010).
[18] T. Dietl, H. Ohno, F. Matsukura, J. Cibert, and D. Ferrand, Science **287**, 1019 (2000).
[19] T. Dietl, H. Ohno, and F. Matsukura, Phys. Rev. B **63**, 195205 (2001).
[20] J. Okabayashi, A. Kimura, O. Rader, T. Mizokawa, A. Fujimori, T. Hayashi, and M. Tanaka, Phys. Rev. B **64**, 125304 (2001).
[21] K. Sato and H. Katayama-Yoshida, Semicond. Sci. Technol. **17**, 367 (2002).
[22] K. S. Burch, D. B. Shrekenhamer, E. J. Singley, J. Stephens, B. L. Sheu, R. K. Kawakami, P. Schiffer, N. Samarth, D. D. Awschalom, and D. N. Basov, Phys. Rev. Lett. **97**, 087208 (2006).
[23] S. Ohya, K. Takata, and M. Tanaka, Nat. Phys. **7**, 342 (2011).
[24] S. Sun, Y. Sun, Z. Liu, D.-I. Lee, S. Peterson, and P. Pianetta, Appl. Phys. Lett. **88**, 021903 (2006).
[25] P. Blaha, K. Schwarz, G. Madsen, D. Kvasnicka, and J. Luitz, *WIEN2K: An Augmented Plane Wave + Local Orbitals Program for Calculating Crystal Properties* (Karlheinz Schwarz, Technische Universität Wien, Vienna, Austria, 2001).
[26] F. Tran and P. Blaha, Phys. Rev. Lett. **102**, 226401 (2009).
[27] J. P. Perdew, K. Burke, and M. Ernzerhof, Phys. Rev. Lett. **77**, 3865 (1996).
[28] G. van der Laan and I. W. Kirkman, J. Phys. Condens. Matter **4**, 4189 (1992).
[29] See Supplemental Material at http://link.aps.org/supplemental/10.1103/PhysRevB.95.075203 for additional information on RPES spectra, constant initial state spectra, and resonance ARPES spectra.
[30] M. R. Thuler, R. L. Benbow, and Z. Hurych, Phys. Rev. B **26**, 669 (1982).
[31] M. Kobayashi, I. Muneta, Y. Takeda, Y. Harada, A. Fujimori, J. Krempaský, T. Schmitt, S. Ohya, M. Tanaka, M. Oshima, and V. N. Strocov, Phys. Rev. B **89**, 205204 (2014).
[32] S. Souma, L. Chen, R. Oszwałdowski, T. Sato, F. Matsukura, T. Dietl, H. Ohno, and T. Takahashi, Sci. Rep. **6**, 27266 (2016).
[33] K. Momma and F. Izumi, J. Appl. Crystallogr. **44**, 1272 (2011).
[34] H. Weng and J. Dong, Phys. Rev. B **71**, 035201 (2005).